NeuroImage 93 (2014) 252–259

Contents lists available at ScienceDirect

NeuroImage

journal homepage: www.elsevier.com/locate/ynimg

Review

MRI parcellation of *ex vivo* medial temporal lobe

Jean C. Augustinack [a,*], Caroline Magnain [a], Martin Reuter [a], André J.W. van der Kouwe [a], David Boas [a], Bruce Fischl [a,b]

[a] Athinoula A Martinos Center, Dept. of Radiology, MGH, 149 13th Street, Charlestown, MA 02129, USA
[b] MIT Computer Science and AI Lab, Cambridge, MA 02139, USA

ARTICLE INFO

Article history:
Accepted 8 May 2013
Available online 21 May 2013

Keywords:
Entorhinal
Brodmann's area 28
Perirhinal
Brodmann's area 35
Mapping
Localization

ABSTRACT

Recent advancements in radio frequency coils, field strength and sophisticated pulse sequences have propelled modern brain mapping and have made validation to biological standards – histology and pathology – possible. The medial temporal lobe has long been established as a pivotal brain region for connectivity, function and unique structure in the human brain, and reveals disconnection in mild Alzheimer's disease. Specific brain mapping of mesocortical areas affected with neurofibrillary tangle pathology early in disease progression provides not only an accurate description for location of these areas but also supplies spherical coordinates that allow comparison between other *ex vivo* cases and larger *in vivo* datasets. We have identified several cytoarchitectonic features in the medial temporal lobe with high resolution *ex vivo* MRI, including gray matter structures such as the entorhinal layer II 'islands', perirhinal layer II–III columns, presubicular 'clouds', granule cell layer of the dentate gyrus as well as lamina of the hippocampus. Localization of Brodmann areas 28 and 35 (entorhinal and perirhinal, respectively) demonstrates MRI based area boundaries validated with multiple methods and histological stains. Based on our findings, both myelin and Nissl staining relate to contrast in *ex vivo* MRI. Precise brain mapping serves to create modern atlases for cortical areas, allowing accurate localization with important applications to detecting early disease processes.

Contents

Introduction

This review on the MRI parcellation of *ex vivo* medial temporal lobe outlines the importance of accurate localization, summarizes the critical advantages of *ex vivo* brain mapping, and describes the architectural features used to delineate them. This review also discusses *ex vivo* contrast and details the pattern of neuropathological markers that affect the cortical ribbon in the medial temporal lobe.

In 1909, Brodmann published his cytoarchitectonic map and it is hard to believe that a hundred years later it still serves as the standard in structural and neuroanatomical brain mapping (Brodmann, 1909). The Brodmann map accurately distinguishes cortical areas of the cerebrum. Brodmann's map withstood the test of time because

* Corresponding author at: Athinoula A Martinos Center, Massachusetts Gen. Hosp/Harvard Med. School, Bldg. 149, 13th St., Charlestown, MA 02129, USA. Fax: +1 617 726 7422.
E-mail address: jean@nmr.mgh.harvard.edu (J.C. Augustinack).

1053-8119/$ – see front matter © 2013 Elsevier Inc. All rights reserved.
http://dx.doi.org/10.1016/j.neuroimage.2013.05.053

it defined 52 areas based on laminar organization, the presence or absence of cells, cell density neuronal size and shape. Likely due to the massive undertaking of such a project, Brodmann's comments about each area were relatively sparse. He left many details for future anatomists to describe. Substantial progress has been made, and comparable to Brodmann's work, a similar mission has begun for brain mapping in neuroimaging. The task to define cortical areas architectonically, validate and apply to an MRI reconstruction has been cultivated in modern brain mapping.

In biology, structure usually dictates function. The accurate localization of structural features in an architectonic or MRI approach facilitates our understanding of specific brain function. The medial temporal lobe plays a critical role in memory, emotion, olfaction and the convergence of multimodal association areas. The hippocampus, dentate gyrus, amygdala and overlying parahippocampal gyrus are medial temporal lobe structures that subserve an array of functions (Van Hoesen, 1995). Entorhinal (Brodmann's area 28) and perirhinal (Brodmann's area 35) cortices make up the anterior half of the parahippocampal gyrus, entorhinal on the crown and perirhinal in the depths of the rhinal and collateral sulci. The entorhinal and perirhinal cortices are collectively referred to as mesocortices of the parahippocampal gyrus and these cortical areas will be the focus of this review.

When the memory circuitry in the medial temporal lobe region undergoes neuropathological changes, memory competencies degrade and advanced Alzheimer's disease follows. Alzheimer's disease severely affects the cerebral cortex but also involves limbic structures such as the hippocampus, amygdala and septal/basal forebrain region. Neuropathological markers in Alzheimer's disease – neurofibrillary tangles and senile plaques – manifest throughout the cerebral cortex, although in different places, densities and timing. Beta-amyloid plaques develop early in the disease primarily in parietal cortex, while neurofibrillary tangles, composed of hyper-phosphorylated tau, manifest later in perirhinal and entorhinal cortices (Arnold et al., 1991b; Braak and Braak, 1991; Kordower et al., 2001; Van Hoesen et al., 2000). These mesocortices of the medial temporal lobe display the first site of neurofibrillary tangles in the human brain (Braak and Braak, 1995). With the demise of these critical areas, when entorhinal and perirhinal fall to neurofibrillary tangles, the hippocampus becomes isolated and the resultant memory damage is not reversible (Hyman et al., 1984). Thus, neurofibrillary tangles and neuronal loss strongly correlate with dementia (Arriagada et al., 1992; Gomez-Isla et al., 1997; Savva et al., 2009).

Given its critical clinical and neuroscientific significance, precise identification of medial temporal lobe area boundaries is essential in modern neuroimaging. Past neuroimaging methods have relied on sulcal and gyral topography and morphometry. Anyone who has ever worked with or studied the human brain understands the challenges that arise due to the enormous variability of the gyri and sulci, especially in higher association cortical areas (Fischl et al., 2001; Fischl et al., 2008; Ono et al., 1990; Van Essen, 1997). Using topographic or volumetric registration to an atlas coordinate system (Talairach and Tournoux, 1988) has become outdated. As neuroimaging assessment becomes more sophisticated with specific cortical thickness measures and laminar sampling, better outcome measures result. Surface and laminar based brain mapping offers a much improved scenario from the global volumetric changes that were advanced only a decade ago.

Ex vivo imaging has advanced as an important brain mapping technique due to several reasons. The *ex vivo* imaging model enables the two best parts of the neuroimaging and biology – the ability to make surfaces and basic histologic staining – and combines them. Thus, the *ex vivo* model pulls in the biological components, whether that is cytoarchitectural, myeloarchitectural, chemoarchitectural or even pathoarchitectural (Amunts and Zilles, 2001; Amunts et al., 2005; Augustinack et al., 2005; Augustinack et al., 2013; Eickhoff et al., 2005; Geyer et al., 2011; Morosan et al., 2005), and applies this validation to a surface reconstruction and this surface reconstruction may be applied to *in vivo* datasets (Augustinack et al., 2013; Fischl et al., 2009). *Ex vivo* modeling allows validation of area boundaries for precise and accurate localization and enables the future application to multiple datasets based on histological verification. *Ex vivo* models are constructed from high resolution imaging with custom radio frequency coils and long motionless scan sessions (Augustinack et al., 2005; Blamire et al., 1999; Nagara et al., 1987; Pfefferbaum et al., 2004). The resultant images detail architectonic properties once reserved for the biologist only.

The objective of this review is to highlight the architectonic features observed in the medial temporal lobe using *ex vivo* methods to define its boundaries and pass along lessons learned for *ex vivo* modeling in neuroanatomy and neuroimaging.

General procedure

A few important attributes in human brain samples are noteworthy for *ex vivo* imaging. While it's difficult to narrow down exactly what traits give good *ex vivo* contrast in a practical sense, a couple of items have emerged from our personal experience using this model (Augustinack et al., 2005, 2010, 2013; Fischl et al., 2009). Here, we list a few specific lessons that we have learned from our *ex vivo* investigations. First, the brain must be fully fixed to avoid artifacts. If not, a fixation artifact will show a difference in contrast where the brain is fixed on the outer cortical areas but not fixed in the interior of the white matter and subcortical areas. Thorough fixation requires approximately 4 weeks depending on the strength of the fixative. A standard protocol is typically 10% formalin. Second and related, the samples must be fairly recently fixed (less than one year). A brain that has been fixed for years will not generate good *ex vivo* contrast. For fixation, a time frame between two months and one year reveals the optimal *ex vivo* contrast. The third trait relates to post-mortem interval (the time between death and tissue fixation). It is unclear to what degree post-mortem interval time contributes to good *ex vivo* contrast. Generally, post-mortem interval times are limited to less than 24 h. Shorter post-mortem interval times such as 6 h have not affected or significantly improved *ex vivo* contrast, but this evidence remains to be fully documented.

A typical *ex vivo* neuroimaging protocol is different than an *in vivo* protocol. The most outstanding difference centers on the fact that fixation changes the contrast. T1 is shortened in *ex vivo* imaging, especially in gray matter (Blamire et al., 1999; Nagara et al., 1987; Pfefferbaum et al., 2004; Tovi and Ericsson, 1992), and little T1 contrast remains between gray and white matter. T2* contrast dominates the *ex vivo* image (Dawe et al., 2009; Tovi and Ericsson, 1992), while *in vivo* contrast relies to a greater extent on T1. Fast low angle shot (FLASH, Siemens, Erlangen Germany) images display exquisite neuroanatomical detail for *ex vivo* brains. The FLASH sequence (or spoiled gradient echo (SPGR) for GE scanners) with appropriate choice of timing parameters and radio frequency (RF) and flip angle, generates images with a favorable combination of T2* and proton density contrasts. For high resolution *ex vivo* imaging, a relatively long echo time enhances T2* contrast. In our optimization using the steady-state Bloch equations (Bloch, 1946), we have estimated that a flip angle of approximately 20° with a TR/TE of 40/20 ms produces optimal FLASH contrast for visualizing anatomical properties at 7 T. Finally, collecting three to four volumes reduces noise and enables one to observe architectonic structures that are well beyond our ability to detect *in vivo*. Each volume is approximately 1.5 h.

Custom radio frequency coils have had a significant impact on high-resolution neuroimaging in ex vivo acquisitions and experiments. Specialized surface array coils (typically 4–8 coils) help collect the standard resolution images (1 mm^3) of the entire hemisphere, while efficient solenoid coils that encompass the sample entirely boost SNR and enable ultra-high resolution ($\leq$100 μm^3) images. High-resolution images can also be collected with surface array coils but the solenoid coils offer superior contrast to noise ratios relative to phased-array coils.

Practical issues emerge with *ex vivo* imaging and these issues must be addressed. Notably, in the *ex vivo* model, the brain is removed from the skull, immersed in fixative liquid and packed in a holder or bag during scanning. Given this, bubbles can occur. If the pia matter remains intact, more bubbles are trapped in this membrane. For a hemisphere scan, it is nearly impossible to extricate every bubble, a particular problem at the high field strengths (*e.g.* 7.0 T) needed to obtain high-resolution images of the anatomy. Removal of the pia mater with careful and gentle dissection is recommended before MRI scanning. In addition, packing the sample in a holder the day prior to the scanning has helped decrease the number of bubbles. Careful handling of the brain and surrounding liquid is necessary to avoid generating new bubbles once packed. The bubbles are less of a problem for the smaller excised blocks typically scanned in a solenoid coil. These tissue samples are generally small enough to void all bubbles. The other issue to be aware of is the orientation of the orthogonal planes. If the brain is carefully positioned in the scanner, that is helpful. If not, the brain hemisphere requires reorientating so that all structures appear in the coronal orientation that anatomists are accustomed to. The arbitrary planes (other than coronal, axial and sagittal) offer many additional views in brain organization, especially with high-resolution detail using *ex vivo* tissue and can be quite educational. Finally, the MR images and histologically stained tissue must be registered if we wish to relate histological properties to MRI ones. Histological processing and staining involve physical manipulation such as mounting tissue by hand onto slides and tissue dehydration before cover slipping, thus the histology section undergoes tremendous change compared to the MRI images. For this reason, a set of blockface images is collected during sectioning. A blockface image is a photograph of the fixed but unstained gross tissue at each slice, acquired before sectioning with a sliding microtome. Thus, there is one blockface for each histological section. The blockface image (Fig. 1B) acts as an intermediary between the MRI (Fig. 1A) and histological tissue images (Fig. 1C) for registration. Another advantage of the blockface volume is that it is fully 3D and does not contain interruptions, as do the histology slices. Histological slices are typically stained in series (*e.g.* every 10th section) and therefore each consecutive section is not stained with the same histochemical dye. Our registration method follows these critical steps (Reuter et al., 2012). First, the blockface (foreground) is segmented from the surrounding dry ice background (Ceritoglu et al., 2010). All images are normalized (Wachinger, 2010). The blockface is registered with the MRI with linear registration followed by non-linear registration (Sand and Teller, 2008). Then, each MRI slice is extracted from the non-linear registration for each respective blockface image. Subsequently each histological slice is (both linearly and then non-linearly) registered to the corresponding MR slice. Thus, the blockface to MRI registration is fully 3D while the registration of each histological slice to the MRI is 2D.

Probabilistic mapping techniques

Probabilistic mapping analyses include several steps to generate the final prediction of the cortical field. Two MRI scans are acquired; one of the excised tissue block at ultra-high resolution (100 μm^3 isotropic, 7.0 T, fast-low-angle-shot sequence, TE = 20 ms, TR = 40 ms, flip angles 15°, 20° and 25°, three image averages for each flip angle) (Fig. 2A) and the other of the entire hemisphere with a standard resolution (1 mm isotropic, 1.5 T, a multi-echo fast-low-angle-shot sequence, TR = 20 ms, TE = 1.85 + n × 2.0 ms, n = 0, …, 7 and flip angle = 20°) (Fig. 2C). Acquisitions with different flip angles were used to invert the steady state Bloch equations and estimate T1/T2*/PD, and form a single volume with a high SNR/CNR (Fischl et al., 2004). Once the cortical field and its laminar properties are identified, a label is drawn to delineate the area boundary (Fig. 2B). This manual labeling is performed throughout the rostrocaudal extent. Perirhinal area 35 is the example used in this figure and is labeled in blue along the medial bank of the collateral sulcus (Fig. 2B). Once the entire anterior–posterior extent of the cortical area is labeled, the label is transformed from the 100 μm^3 MRI to 1 mm^3 MRI of the entire hemisphere (Fig. 2C), where the 1 mm is sampled onto surface models and used to create the probabilistic map on a spherically warped FreeSurfer average. For this affine registration, Register in the MNI toolkit MNI toolkit, Montreal, Canada, (http://www.bic.mcgill.ca) is used to obtain correspondence between the lower resolution image and the higher resolution image with manual fiduciary tags.

Area boundaries

Entorhinal cortex (Brodmann's area 28) boundaries

The architecture of the entorhinal cortex has been well studied with traditional neuroanatomical methods (Augustinack et al., 2005; Braak and Braak, 1992; Cajal, 1995; Fischl et al., 2009; Insausti et al., 1995; Krimer et al., 1997; Lorente de No, 1933; Van Hoesen, 1995; Van Hoesen and Solodkin, 1993) and *ex vivo* MRI (Augustinack et al., 2005; Fischl et al., 2009). Entorhinal cortex borders parasubiculum on its medial side and perirhinal cortex (area 35) on its lateral side. Entorhinal cortex exhibits a cortical organization that is unique. Neurons of layer II cluster and form neuronal rich islands and neuron-sparse inter-islands. Large multiple polar (*i.e.* stellate) and pyramidal neurons comprise the second lamina. The entorhinal islands can be observed on 100 μm^3 *ex vivo* MRI and embody a substantial part of the supragranular lamina of entorhinal cortex, displaying a bright intensity on FLASH images (Fig. 3A) but a dark chromophilic contrast in Nissl stained tissues (Fig. 3B). Entorhinal cortex lamina III contains small pyramidal neurons and is relatively wide. Lamina dissecans is a

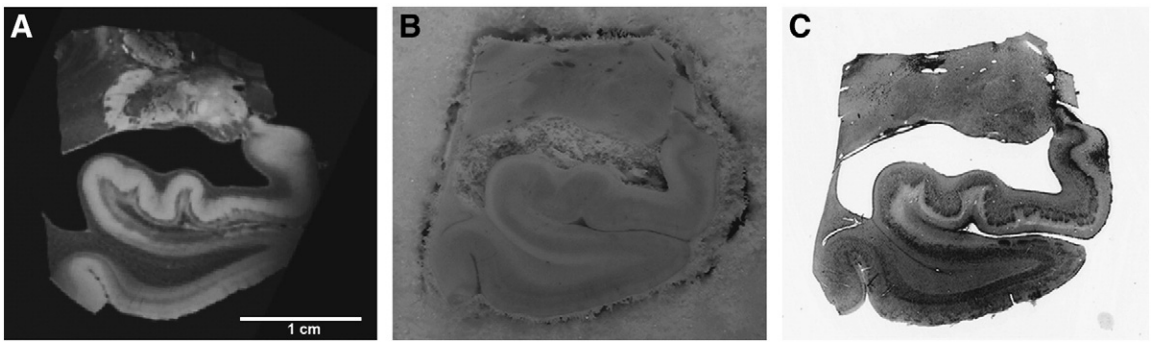

Fig. 1. *Ex vivo* MRI (A), blockface (B) and Nissl stained section (C). Blockface images, collected serially during sectioning, aid in the registration between *ex vivo* MRI and histological slice.

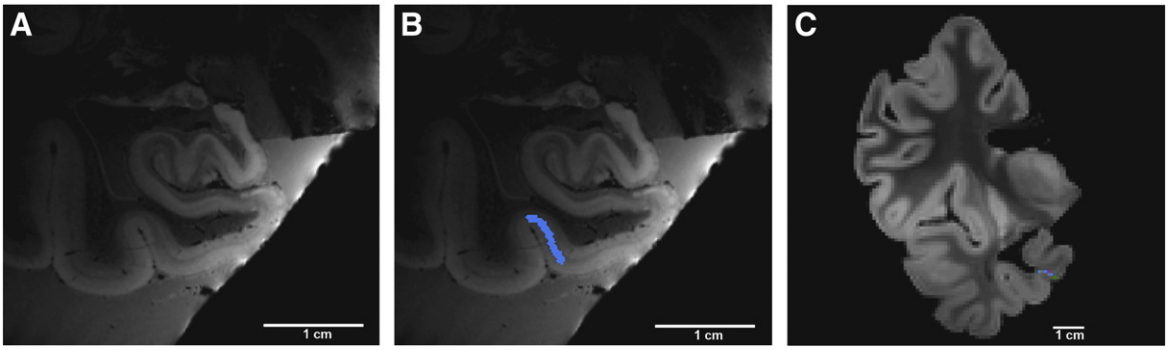

Fig. 2. Steps in the *ex vivo* probabilistic mapping pipeline. High-resolution, high field detection of cortical architectonic fields in *ex vivo* MRI (A). Region of interest labeled throughout rostrocaudal extent (blue label = perirhinal area 35 as example) in (B). High resolution label transformed onto low resolution volume in (C). Note blue label in medial bank of collateral sulcus in lower resolution image.

cell free zone between the supragranular and infragranular layers in entorhinal cortex. The lamina dissecans layer produces a dark contrast in the FLASH images (Fig. 3A). Lamina IV in entorhinal cortex contains medium sized pyramidal neurons. This layer receives inputs from CA1/subiculum of the hippocampus. Layers IV, V and VI display relatively homogenous contrast on FLASH *ex vivo* MRI. Layers V and VI are closely opposed and difficult to distinguish even under the microscope.

In general, the entorhinal cortex is not heavily myelinated. However, there are several distinct myelinated structures to note. The infragranular layers have more myelin than the supragranular layers. A light hue of myelin is stained in the infragranular layers just inferior to the angular bundle (the white matter of parahippocampal gyrus) (Fig. 3C). Additional medial temporal lobe structures that are further downstream of entorhinal cortex are highlighted in the Gallyas staining, notably the hippocampus and subiculum (Fig. 3C). Moderate myelination occurs at the presubiculum where the perforant pathway (of layers II and III of entorhinal cortex) fibers project through the subicular cortex to arrive at the distal one third of the dendrites of the dentate gyrus and CA3 hippocampal neurons. The layer II neurons project via the perforant route but also use the temporal alvear pathway to the hippocampus. The alveus (mostly dorsal to hippocampus) and superficial presubicular pathway (dorsal to presubiculum) both show robust myelin staining. In Fig. 3, the myelin staining (Fig. 3C) corresponds well with the dark contrast in FLASH MRI (Fig. 3A).

The features that define area boundaries frequently follow general cortical divisions, which include allocortex (or paleocortex), periallocortex, proisocortex and isocortex. Allocortical (hippocampal) and paleocortex (olfactory cortex) each have three layers. Periallocortex contains six layers and is the oldest cortex that has six layers. Periallocortex is agranular cortex and includes parasubiculum, presubiculum, entorhinal and perirhinal area 35a. Next, proisocortex is dysgranular cortex and perirhinal area 35b portrays the prime example in the medial temporal lobe. The dysgranular description of layer IV implies variability where layer IV is transitioning from agranular to granular cortex. Isocortex is the newest evolutionary cortex and accounts for the vast majority of cerebral cortex in the human brain. Temporal isocortical area 36 borders the medial temporal lobe laterally and is an example of isocortex (Gloor, 1997; Van Hoesen et al., 2000).

Perirhinal cortex (Brodmann's area 35) boundaries

The architecture of the perirhinal cortex has been described with traditional histological methods (Augustinack et al., 2013; Braak and Braak, 1985; Ding and Van Hoesen, 2010; Ding et al., 2009; Insausti et al., 1998; Taylor and Probst, 2008; Van Hoesen, 1995; Van Hoesen and Solodkin, 1993; Van Hoesen et al., 2000) and *ex vivo* MRI (Augustinack et al., 2013). For the majority of its domain, perirhinal cortex borders entorhinal cortex medially and has the temporal isocortex area 36 as its lateral neighbor. Of course, neuroanatomy is rarely simple. Anteriorly, piriform cortex borders the perirhinal cortex medially and temporal isocortical area 36 borders perirhinal area 35 laterally. Layers II and III in area 35a organize into vertical columns and elongate laterally. The dark oblique band in FLASH MRI reveals the elongation of layers II and III in area 35a (Fig. 3A). This same band is extremely faint but present in the myelin stained section (Fig. 3C). The neuronal size in layer II in 35 is smaller than entorhinal layer II neurons. Layer IV in area 35a is agranular and contains no cells. Layer V is unorganized but is composed of medium sized pyramidal neurons in area 35a.

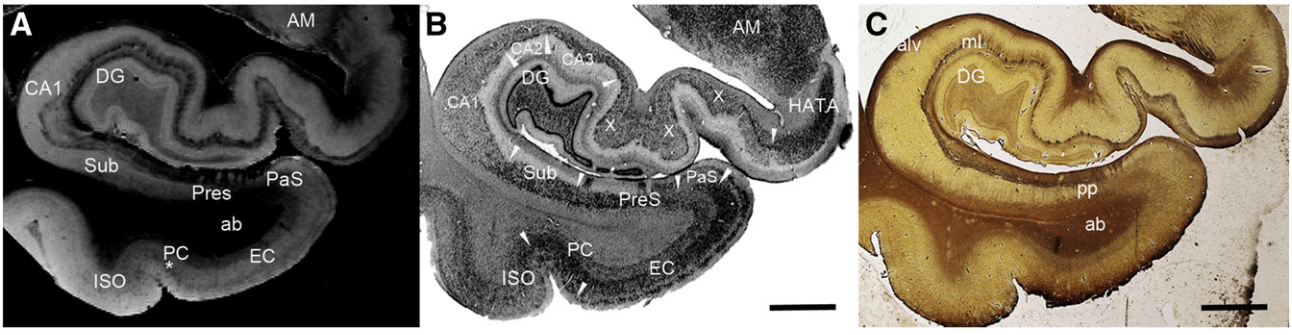

Fig. 3. *Ex vivo* MRI (A), Nissl (B) and Myelin stained sections (C). Note the contrast correspondence to MRI in both the cortical gray matter in Nissl (B) and also the white matter myelinated fibers in (C). White arrowheads designate area boundaries. Abbreviations: ab = angular bundle, alv = alveus, AM = amygdala, CA1–CA3 = subfields of cornu ammonis, DG = dentate gyrus, EC = entorhinal cortex, HATA = hippocampal-amygdala transition area, ISO = isocortical Brodmann's area 36, ml = molecular layer, pp = perforant pathway, PC = perirhinal cortex, PaS = parasubiculum, PreS = presubiculum, Sub = subiculum, X = mixture of CA1 and CA2 due to an oblique plane of cut, * = unique layer in perirhinal cortex, Brodmann's area 35. Magnification bars = 0.5 cm.

As noted above, area 35a is characteristic of periallocortex as is entorhinal area 28, but perirhinal area 35b represents proisocortex. Layer II neurons in 35b are smaller than area 35a and lose the columnar pattern in superficial layers. Layer III consists of small pyramidal neurons while layer IV in 35b exhibits a dysgranular organization. Layer V in 35b becomes organized with a thin but distinct pyramidal layer. The dark intensity in the deep layers in area 35b represents the chromophilic medium sized pyramidal neurons of layer V. Layer VI is closely opposed to V and consists of polymorphic neurons. Here, contrast of layers III and V begins to resemble isocortical internal and external pyramidal layers, but not fully organized until temporal isocortical area 36. The contrast in *ex vivo* MRI is higher in the deeper layers in isocortical area 36. Together, the cytoarchitectural lamina and the myeloarchitectural fibers validate the contrast observed in *ex vivo* MRI.

Mapping perirhinal and entorhinal cortices

Once the perirhinal (n = 14) and entorhinal (n = 17) labels were validated with Nissl and (Gallyas) myelin staining, the individual cases were mapped collectively to an existing FreeSurfer template (fsaverage) (Fig. 4). Fig. 4 shows a ventromedial view of the right and left hemisphere averages for the perirhinal (A and B) and entorhinal cortices (C and D). Upon visual inspection, it is evident that the perirhinal average displays greater variability. This finding was demonstrated in our previous publications where the Hausdorff distance showed greater variability in perirhinal cortex than entorhinal cortex (Augustinack et al., 2013; Fischl et al., 2009). The predictability of entorhinal cortex may be due to its location as the first ring of cortex away from the hippocampal fissure and that perirhinal lies exclusively in the depths of the rhinal and collateral sulci. More specifically, perirhinal area 35 lies lateral to the rhinal sulcus and medial to the collateral sulcus. However, the variability in the perirhinal cortex may also be due to fewer subjects (n = 14) than the entorhinal study (n = 17). Although entorhinal predicted location has less variability, cortical thickness measures are complicated by the presence of the tentorium cerebelli. Current T1-weighted *in vivo* MRI does not easily distinguish tissue and dura, requiring additional image types with T2 or T2*-weighted contrast. The perirhinal cortex may be a better marker for changes in mild cognitive impairment or early Alzheimer's changes because perirhinal is not close to the dura and the first neurofibrillary tangles manifest here. One final comment, to strengthen the medial temporal lobe boundary determinations — between parasubiculum and entorhinal, the boundary between entorhinal and perirhinal and the boundary between perirhinal and temporal isocortical area 36, one can look to patho-architecture as well. In mesocortices (perirhinal and entorhinal cortices), neurofibrillary tangles occur in normal non-demented aging (albeit significantly fewer in number) (Bennett et al., 2006; Braak and Braak, 1985; Knopman et al., 2003)and Alzheimer's disease (Arnold et al., 1991a; Braak and Braak, 1991; Van Hoesen and Solodkin, 1993). Early neurofibrillary tangles distinctly demarcate medial temporal lobe boundaries and manifest in entorhinal islands, perirhinal columns and at later stages in temporal isocortical layers III and V (Van Hoesen et al., 2000). The pattern of neurofibrillary tangles in mild Alzheimer's disease provides an additional marker to elucidate area boundaries in the medial temporal lobe.

Nomenclature

In some non-human primate studies, the perirhinal cortex was defined as Brodmann's areas 35 *and* 36 (Buckley and Gaffan, 1997, 1998a, 1998b; Suzuki and Amaral, 1994a, 1994b). In another instance, entorhinal (area 28) and perirhinal (area 35) cortices were grouped together as rhinal cortex (Eacott et al., 1994; Meunier et al., 1996; Murray and Mishkin, 1986). In either case, confusion has occurred and the exact function of area 35 in the primate brain remains unknown. It is anticipated that with accurate localization of more

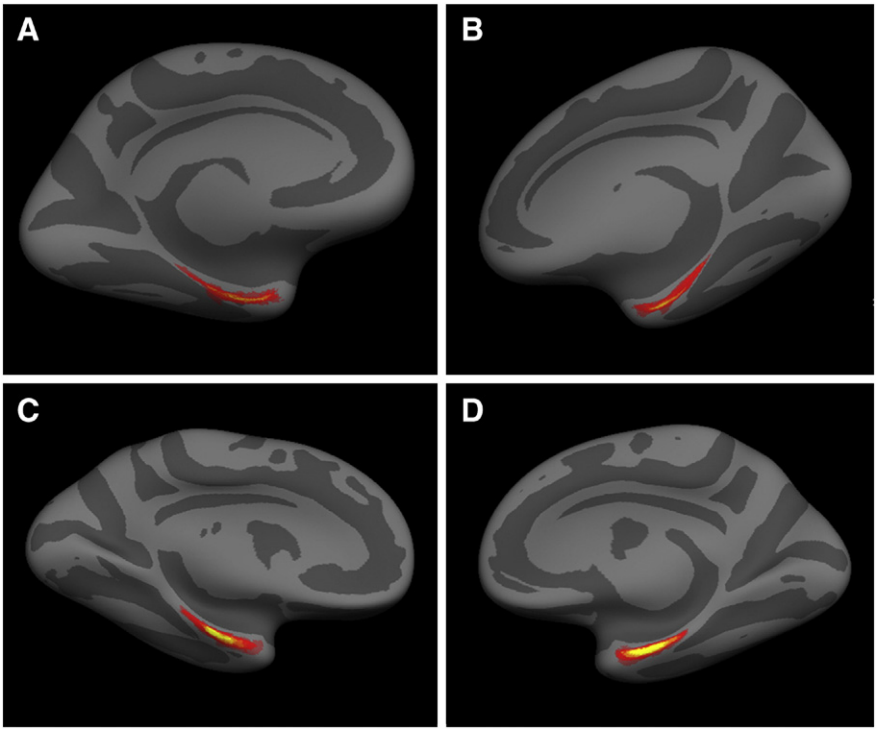

Fig. 4. Left and right hemisphere averages in perirhinal (A and B) and entorhinal (C and D) cortices mapped onto a spherical template. Red and yellow reflect overlapping labels from individual cases.

specific cortical areas (*e.g.* area 35 alone)(Augustinack et al., 2013), functional imaging studies may elucidate more precise functions.

Ex vivo MRI contrast

It is important to discuss what exactly accounts for contrast in *ex vivo* brains. *Ex vivo* contrast is predominately provided by T2 and proton density weighting (Eickhoff et al., 2005; Fukunaga et al., 2010; Tovi and Ericsson, 1992) but T1 (Bock et al., 2009; Geyer et al., 2011) and susceptibility weighted phase contrast also contribute (Duyn et al., 2007; Langkammer et al., 2012). The FLASH image contains multiple types of contrast but it is dominated by T2* and PD through our choice of flip angle, TR and TE. Although myelin likely forms the biophysical source for the majority of *ex vivo* contrast, it could be argued that both fibers and organization of cells account for *ex vivo* contrast, given that the MRI resembles the Nissl stain and myelin stain. Moreover, the fact that the myelin staining of the oblique slant in perirhinal cortex is so light, suggests that factors other than myelin contribute to the observed contrast. Additionally, fiber orientation may aid the visibility of neuroanatomical boundaries and help determine another dimension of contrast (Cohen-Adad et al., 2012; Duyn et al., 2007; Lee et al., 2010, 2011, 2012; Wharton and Bowtell, 2012). As additional analyses are added to the validation of structural features and contrast in *ex vivo* imaging, the brain mapping field will benefit in its specificity and complementation.

The current method rests on the fact that the histology validates the MRI. It is interesting to postulate whether MRI may supersede histological examination of the post-mortem brain. The visualization of the cortical architecture in the medial temporal lobe has an advantage that these cortices display strong modularity. The modularity of structures in the medial temporal lobe, the relative large size of neurons and the abrupt change in laminar pattern helps considerably to demarcate its cortical boundaries. It has been our experience that correspondence between the *ex vivo* MRI and the ground truth histology in the entorhinal and perirhinal cortices is reliable and histology is not required to delineate boundaries in a new case. The last statement has two exceptions, 1) a particularly large cortical area (or large brain) may exceed the region of maximum sensitivity of the solenoid coil, resulting in signal loss at the far ends of the sample, 2) occasionally, brain specimens have poor *ex vivo* contrast for known (greater than one year fixation) and unknown reasons (general variability of human tissue). Thus, *ex vivo* MRI provides an excellent approach to characterize and validate histological properties of medial temporal lobe but other cortical areas with more subtle boundaries create a challenge and may require better contrast and resolution to distinguish boundaries. Considerable technical advances will be needed to achieve sufficient resolution and appropriate contrast to match these results *in vivo*, especially in the deep medial structures of the temporal lobe.

Future work

Histologically stained tissue provides critical validation to MRI slices. However, histology is limited to 2D slices. Obtaining high quality histological images in 3D is an attractive alternative and optical coherence tomography may provide such a solution. Optical coherence tomography is an optical technique that uses the backscattering of light, detects the scattering and resolves structural differences between different tissue types (Huang et al., 1991). Recent studies in *in vivo* rodent models have correlated optical properties and laminar architecture (Srinivasan et al., 2012). Optical coherence tomography has the ability to achieve high resolution and acquire undistorted three-dimensional images over multiple centimeters of brain, when combined with scanning and cutting procedures (Ragan et al., 2012). Collecting architectural data in depth (the third dimension) is an exciting prospect and a feat that is not possible with traditional histology. Fig. 5 shows the boundary between entorhinal and perirhinal cortex but also beautifully demonstrates the perirhinal subdivisions, areas 35a and 35b. The average intensity projection image is somewhat analogous to a neuronal stain in histochemistry where differences in cell density are shown (*i.e.* a Nissl stain) and the maximum intensity projection (MIP) image is analogous to a fiber stain (*i.e.* Gallyas myelin) but can also show individual cells. The cell dense areas appear white in both the maximum intensity projection and average intensity images (Figs. 5A and B). The cell dense areas are especially notable in layers II and IV in entorhinal cortex and layers II and III in perirhinal cortex. The oblique layer is a classic attribute of area 35 and shows a dark contrast in the sum and MIP images. It is interesting to note that the continuity of layer IV in entorhinal cortex extends well into perirhinal 35a suggesting that area 35a truly is a transitional cortex. The MIP optical coherence tomography image shows the orientation of fibers at the entry to the temporal lobe and perirhinal cortex.

Conclusion

Precise localization of cortical areas – specifically entorhinal and perirhinal cortices – will benefit future aging and Alzheimer's analyses as well as basic science in functional and behavioral studies. These mesocortices contain the neurons that manifest neurofibrillary tangles in the human brain. Changes that occur throughout the aging continuum may be mapped specifically to subdivisions of cortical areas. Brodmann would be pleased.

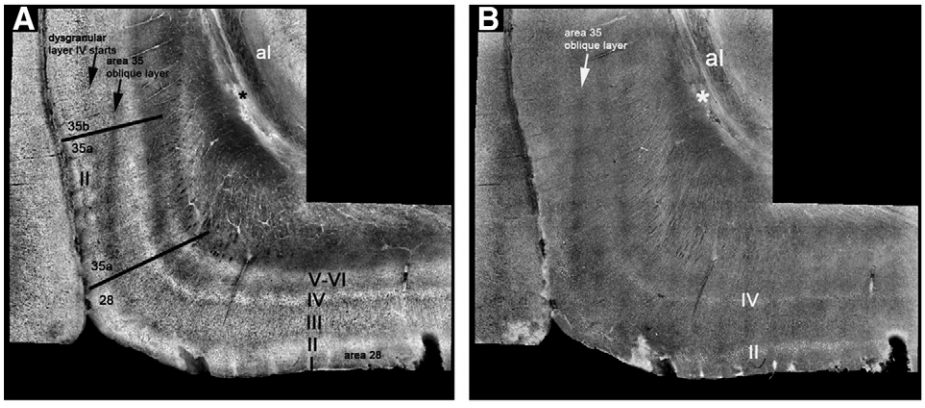

Fig. 5. Optical coherence tomography images shown as an average (A) and maximum intensity projection (B). Optical coherence tomography reveals laminar detail and delineates the area 28, as well as area 35a and area 35b boundaries in the parahippocampal coronal slice.

Acknowledgments

The authors would like to thank Kristen Huber and Sita Kakunoori for technical support. Support for this research was provided in part by the National Center for Research Resources (P41-RR14075, and the NCRR BIRN Morphometric Project BIRN002, U24 RR021382), the National Institute for Biomedical Imaging and Bioengineering (R01EB006758), the National Institute on Aging (K01AG028521, AG022381, 5R01AG008122-22), the National Center for Alternative Medicine (RC1 AT005728-01), the National Institute for Neurological Disorders and Stroke (R01 NS052585-01, 1R21NS072652-01, 1R01NS070963), and was made possible by the resources provided by Shared Instrumentation Grants 1S10RR023401, 1S10RR019307, and 1S10RR023043. Additional support was provided by The Autism & Dyslexia Project funded by the Ellison Medical Foundation, and by the NIH Blueprint for Neuroscience Research (5U01-MH093765), part of the multi-institutional Human Connectome Project.

Conflict of interest

The authors have no conflict of interest to disclose regarding this work.

References

Amunts, K., Zilles, K., 2001. Advances in cytoarchitectonic mapping of the human cerebral cortex. Neuroimaging Clin. N. Am. 11, 151–169 (vii).

Amunts, K., Kedo, O., Kindler, M., Pieperhoff, P., Mohlberg, H., Shah, N.J., Habel, U., Schneider, F., Zilles, K., 2005. Cytoarchitectonic mapping of the human amygdala, hippocampal region and entorhinal cortex: intersubject variability and probability maps. Anat. Embryol. (Berl.) 210, 343–352.

Arnold, S.E., Hyman, B.T., Flory, J., Damasio, A.R., Van Hoesen, G.W., 1991. The topographical and neuroanatomical distribution of neurofibrillary tangles and neuritic plaques in the cerebral cortex of patients with Alzheimer's disease. Cereb. Cortex 1, 103–116.

Arnold, S.E., Hyman, B.T., Van Hoesen, G.W., Damasio, A.R., 1991. Some cytoarchitectural abnormalities of the entorhinal cortex in schizophrenia. Arch. Gen. Psychiatry 48, 625–632.

Arriagada, P.V., Growdon, J.H., Hedley-Whyte, E.T., Hyman, B.T., 1992. Neurofibrillary tangles but not senile plaques parallel duration and severity of Alzheimer's disease. Neurology 42, 631–639.

Augustinack, J.C., van der Kouwe, A.J., Blackwell, M.L., Salat, D.H., Wiggins, C.J., Frosch, M.P., Wiggins, G.C., Potthast, A., Wald, L.L., Fischl, B.R., 2005. Detection of entorhinal layer II using 7 Tesla magnetic resonance imaging. Ann. Neurol. 57, 489–494.

Augustinack, J.C., Helmer, K., Huber, K.E., Kakunoori, S., Zollei, L., Fischl, B., 2010. Direct visualization of the perforant pathway in the human brain with ex vivo diffusion tensor imaging. Front. Hum. Neurosci. 4, 42.

Augustinack, J.C., Huber, K.E., Stevens, A.A., Roy, M., Frosch, M.P., van der Kouwe, A.J., Wald, L.L., Van Leemput, K., McKee, A.C., Fischl, B., 2013. Predicting the location of human perirhinal cortex, Brodmann's area 35, from MRI. Neuroimage 64, 32–42.

Bennett, D.A., Schneider, J.A., Arvanitakis, Z., Kelly, J.F., Aggarwal, N.T., Shah, R.C., Wilson, R.S., 2006. Neuropathology of older persons without cognitive impairment from two community-based studies. Neurology 66, 1837–1844.

Blamire, A.M., Rowe, J.G., Styles, P., McDonald, B., 1999. Optimising imaging parameters for post mortem MR imaging of the human brain. Acta Radiol. 40, 593–597.

Bloch, F., 1946. Nuclear induction. Phys. Rev. 70, 460–474.

Bock, N.A., Kocharyan, A., Liu, J.V., Silva, A.C., 2009. Visualizing the entire cortical myelination pattern in marmosets with magnetic resonance imaging. J. Neurosci. Methods 185, 15–22.

Braak, H., Braak, E., 1985. On areas of transition between entorhinal allocortex and temporal isocortex in the human brain. Normal morphology and lamina-specific pathology in Alzheimer's disease. Acta Neuropathol. 68, 325–332.

Braak, H., Braak, E., 1991. Neuropathological stageing of Alzheimer-related changes. Acta Neuropathol. (Berl.) 82, 239–259.

Braak, H., Braak, E., 1992. The human entorhinal cortex: normal morphology and lamina-specific pathology in various diseases. Neurosci. Res. 15, 6–31.

Braak, H., Braak, E., 1995. Staging of Alzheimer's disease-related neurofibrillary changes. Neurobiol. Aging 16, 271–278 (discussion 278–284).

Brodmann, K., 1909. Vergleichende Lokalisationslehre der Groshirnrinde. Verlag von Johann Ambrosius Barth, Leipzig.

Buckley, M.J., Gaffan, D., 1997. Impairment of visual object-discrimination learning after perirhinal cortex ablation. Behav. Neurosci. 111, 467–475.

Buckley, M.J., Gaffan, D., 1998. Perirhinal cortex ablation impairs configural learning and paired-associate learning equally. Neuropsychologia 36, 535–546.

Buckley, M.J., Gaffan, D., 1998. Perirhinal cortex ablation impairs visual object identification. J. Neurosci. 18, 2268–2275.

Cajal, S., 1995. Histology of the Nervous System of Man and Vertebrates. In: Swanson, Neely, Swanson, Larry W. (Eds.), Oxford University Press. Oxford, New York.

Ceritoglu, C., Wang, L., Selemon, L.D., Csernansky, J.G., Miller, M.I., Ratnanather, J.T., 2010. Large deformation diffeomorphic metric mapping registration of reconstructed 3D histological section images and in vivo MR images. Front. Hum. Neurosci. 4, 43.

Cohen-Adad, J., Polimeni, J.R., Helmer, K.G., Benner, T., McNab, J.A., Wald, L.L., Rosen, B.R., Mainero, C., 2012. T(2)* mapping and B(0) orientation-dependence at 7 T reveal cyto- and myeloarchitecture organization of the human cortex. Neuroimage 60, 1006–1014.

Dawe, R.J., Bennett, D.A., Schneider, J.A., Vasireddi, S.K., Arfanakis, K., 2009. Postmortem MRI of human brain hemispheres: T2 relaxation times during formaldehyde fixation. Magn. Reson. Med. 61, 810–818.

Ding, S.L., Van Hoesen, G.W., 2010. Borders, extent, and topography of human perirhinal cortex as revealed using multiple modern neuroanatomical and pathological markers. Hum. Brain Mapp. 31, 1359–1379.

Ding, S.L., Van Hoesen, G.W., Cassell, M.D., Poremba, A., 2009. Parcellation of human temporal polar cortex: a combined analysis of multiple cytoarchitectonic, chemoarchitectonic, and pathological markers. J. Comp. Neurol. 514, 595–623.

Duyn, J.H., van Gelderen, P., Li, T.Q., de Zwart, J.A., Koretsky, A.P., Fukunaga, M., 2007. High-field MRI of brain cortical substructure based on signal phase. Proc. Natl. Acad. Sci. U. S. A. 104, 11796–11801.

Eacott, M.J., Gaffan, D., Murray, E.A., 1994. Preserved recognition memory for small sets, and impaired stimulus identification for large sets, following rhinal cortex ablations in monkeys. Eur. J. Neurosci. 6, 1466–1478.

Eickhoff, S., Walters, N.B., Schleicher, A., Kril, J., Egan, G.F., Zilles, K., Watson, J.D., Amunts, K., 2005. High-resolution MRI reflects myeloarchitecture and cytoarchitecture of human cerebral cortex. Hum. Brain Mapp. 24, 206–215.

Fischl, B., Liu, A., Dale, A.M., 2001. Automated manifold surgery: constructing geometrically accurate and topologically correct models of the human cerebral cortex. IEEE Trans. Med. Imaging 20, 70–80.

Fischl, B., Salat, D.H., van der Kouwe, A.J., Makris, N., Segonne, F., Quinn, B.T., Dale, A.M., 2004. Sequence-independent segmentation of magnetic resonance images. Neuroimage 23 (Suppl. 1), S69–S84.

Fischl, B., Rajendran, N., Busa, E., Augustinack, J., Hinds, O., Yeo, B.T., Mohlberg, H., Amunts, K., Zilles, K., 2008. Cortical folding patterns and predicting cytoarchitecture. Cereb. Cortex 18, 1973–1980.

Fischl, B., Stevens, A.A., Rajendran, N., Yeo, B.T., Greve, D.N., Van Leemput, K., Polimeni, J.R., Kakunoori, S., Buckner, R.L., Pacheco, J., Salat, D.H., Melcher, J., Frosch, M.P., Hyman, B.T., Grant, P.E., Rosen, B.R., van der Kouwe, A.J., Wiggins, G.C., Wald, L.L., Augustinack, J.C., 2009. Predicting the location of entorhinal cortex from MRI. Neuroimage 47, 8–17.

Fukunaga, M., Li, T.Q., van Gelderen, P., de Zwart, J.A., Shmueli, K., Yao, B., Lee, J., Maric, D., Aronova, M.A., Zhang, G., Leapman, R.D., Schenck, J.F., Merkle, H., Duyn, J.H., 2010. Layer-specific variation of iron content in cerebral cortex as a source of MRI contrast. Proc. Natl. Acad. Sci. U. S. A. 107, 3834–3839.

Geyer, S., Weiss, M., Reimann, K., Lohmann, G., Turner, R., 2011. Microstructural parcellation of the human cerebral cortex — from Brodmann's post-mortem map to in vivo mapping with high-field magnetic resonance imaging. Front. Hum. Neurosci. 5, 19.

Gloor, P., 1997. The Temporal Lobe and Limbic System. Oxford University Press, New York, New York.

Gomez-Isla, T., Hollister, R., West, H., Mui, S., Growdon, J.H., Petersen, R.C., Parisi, J.E., Hyman, B.T., 1997. Neuronal loss correlates with but exceeds neurofibrillary tangles in Alzheimer's disease. Ann. Neurol. 41, 17–24.

Huang, D., Swanson, E.A., Lin, C.P., Schuman, J.S., Stinson, W.G., Chang, W., Hee, M.R., Flotte, T., Gregory, K., Puliafito, C.A., et al., 1991. Optical coherence tomography. Science 254, 1178–1181.

Hyman, B.T., Van Hoesen, G.W., Damasio, A.R., Barnes, C.L., 1984. Alzheimer's disease: cell-specific pathology isolates the hippocampal formation. Science 225, 1168–1170.

Insausti, R., Tunon, T., Sobreviela, T., Insausti, A.M., Gonzalo, L.M., 1995. The human entorhinal cortex: a cytoarchitectonic analysis. J. Comp. Neurol. 355, 171–198.

Insausti, R., Insausti, A.M., Sobreviela, M.T., Salinas, A., Martinez-Penuela, J.M., 1998. Human medial temporal lobe in aging: anatomical basis of memory preservation. Microsc. Res. Tech. 43, 8–15.

Knopman, D.S., Parisi, J.E., Salviati, A., Floriach-Robert, M., Boeve, B.F., Ivnik, R.J., Smith, G.E., Dickson, D.W., Johnson, K.A., Petersen, L.E., McDonald, W.C., Braak, H., Petersen, R.C., 2003. Neuropathology of cognitively normal elderly. J. Neuropathol. Exp. Neurol. 62, 1087–1095.

Kordower, J.H., Chu, Y., Stebbins, G.T., DeKosky, S.T., Cochran, E.J., Bennett, D., Mufson, E.J., 2001. Loss and atrophy of layer II entorhinal cortex neurons in elderly people with mild cognitive impairment. Ann. Neurol. 49, 202–213.

Krimer, L.S., Hyde, T.M., Herman, M.M., Saunders, R.C., 1997. The entorhinal cortex: an examination of cyto- and myeloarchitectonic organization in humans. Cereb. Cortex 7, 722–731.

Langkammer, C., Krebs, N., Goessler, W., Scheurer, E., Yen, K., Fazekas, F., Ropele, S., 2012. Susceptibility induced gray–white matter MRI contrast in the human brain. Neuroimage 59, 1413–1419.

Lee, J., Shmueli, K., Fukunaga, M., van Gelderen, P., Merkle, H., Silva, A.C., Duyn, J.H., 2010. Sensitivity of MRI resonance frequency to the orientation of brain tissue microstructure. Proc. Natl. Acad. Sci. U. S. A. 107, 5130–5135.

Lee, J., van Gelderen, P., Kuo, L.W., Merkle, H., Silva, A.C., Duyn, J.H., 2011. T2*-based fiber orientation mapping. Neuroimage 57, 225–234.

Lee, J., Shmueli, K., Kang, B.T., Yao, B., Fukunaga, M., van Gelderen, P., Palumbo, S., Bosetti, F., Silva, A.C., Duyn, J.H., 2012. The contribution of myelin to magnetic susceptibility-weighted contrasts in high-field MRI of the brain. Neuroimage 59, 3967–3975.

Lorente de No, R., 1933. Studies on the structure of the cerebral cortex. J. Psychol. Neurol. 45.

Meunier, M., Hadfield, W., Bachevalier, J., Murray, E.A., 1996. Effects of rhinal cortex lesions combined with hippocampectomy on visual recognition memory in rhesus monkeys. J. Neurophysiol. 75, 1190–1205.

Morosan, P., Schleicher, A., Amunts, K., Zilles, K., 2005. Multimodal architectonic mapping of human superior temporal gyrus. Anat. Embryol. (Berl.) 210, 401–406.
Murray, E.A., Mishkin, M., 1986. Visual recognition in monkeys following rhinal cortical ablations combined with either amygdalectomy or hippocampectomy. J. Neurosci. 6, 1991–2003.
Nagara, H., Inoue, T., Koga, T., Kitaguchi, T., Tateishi, J., Goto, I., 1987. Formalin fixed brains are useful for magnetic resonance imaging (MRI) study. J. Neurol. Sci. 81, 67–77.
Ono, M., Kubik, S., Abernathey, C.D., 1990. Atlas of the Cerebral Sulci. Georg Thieme Verlag, New York.
Pfefferbaum, A., Sullivan, E.V., Adalsteinsson, E., Garrick, T., Harper, C., 2004. Postmortem MR imaging of formalin-fixed human brain. Neuroimage 21, 1585–1595.
Ragan, T., Kadiri, L.R., Venkataraju, K.U., Bahlmann, K., Sutin, J., Taranda, J., Arganda-Carreras, I., Kim, Y., Seung, H.S., Osten, P., 2012. Serial two-photon tomography for automated ex vivo mouse brain imaging. Nat. Methods 9, 255–258.
Reuter, M., Sand, P., Huber, K., Nguyen, K., Saygin, Z., Rosas, H.D., Augustinack, J., Fischl, B., 2012. Registration of histology and MRI using blockface as intermediate space.
Sand, P., Teller, S., 2008. Particle video: long-range motion estimation using point trajectories. Int. J. Comput. Vis. 80, 72–91.
Savva, G.M., Wharton, S.B., Ince, P.G., Forster, G., Matthews, F.E., Brayne, C., 2009. Age, neuropathology, and dementia. N. Engl. J. Med. 360, 2302–2309.
Srinivasan, V.J., Radhakrishnan, H., Jiang, J.Y., Barry, S., Cable, A.E., 2012. Optical coherence microscopy for deep tissue imaging of the cerebral cortex with intrinsic contrast. Opt. Express 20, 2220–2239.
Suzuki, W.A., Amaral, D.G., 1994. Perirhinal and parahippocampal cortices of the macaque monkey: cortical afferents. J. Comp. Neurol. 350, 497–533.
Suzuki, W.A., Amaral, D.G., 1994. Topographic organization of the reciprocal connections between the monkey entorhinal cortex and the perirhinal and parahippocampal cortices. J. Neurosci. 14, 1856–1877.
Talairach, J., Tournoux, P., 1988. Co-planar stereotaxic atlas of the human brain.
Taylor, K.I., Probst, A., 2008. Anatomic localization of the transentorhinal region of the perirhinal cortex. Neurobiol. Aging 29, 1591–1596.
Tovi, M., Ericsson, A., 1992. Measurements of T1 and T2 over time in formalin-fixed human whole-brain specimens. Acta Radiol. 33, 400–404.
Van Essen, D.C., 1997. A tension-based theory of morphogenesis and compact wiring in the central nervous system. Nature 385, 313–318.
Van Hoesen, G.W., 1995. Anatomy of the medial temporal lobe. Magn. Reson. Imaging 13, 1047–1055.
Van Hoesen, G.W., Solodkin, A., 1993. Some modular features of temporal cortex in humans as revealed by pathological changes in Alzheimer's disease. Cereb. Cortex 3, 465–475.
Van Hoesen, G.W., Augustinack, J.C., Dierking, J., Redman, S.J., Thangavel, R., 2000. The parahippocampal gyrus in Alzheimer's disease. Clinical and preclinical neuroanatomical correlates. Ann. N. Y. Acad. Sci. 911, 254–274.
Wachinger, C., 2010. Structural image representation for image registration. Proceedings of IEEE Computer Vision and Pettern Recognition Workshops, pp. 23–30.
Wharton, S., Bowtell, R., 2012. Fiber orientation-dependent white matter contrast in gradient echo MRI. Proc. Natl. Acad. Sci. U. S. A. 109 (45), 18559–18564.